Turkish Journal of Civil Engineering, 2024 125-147, Paper 772, ***Research Article***

Computational Modelling of Damage Progression in Unreinforced Masonry Walls via DEM

Bora PULATSU[1*]
Kagan TUNCAY[2]

ABSTRACT

Unreinforced masonry (URM) walls are the common load-bearing elements for old masonry buildings and heritage structures. As witnessed from the past and recent earthquakes, URM walls may demonstrate various collapse mechanisms along with different crack patterns influenced by the wall aspect ratio, vertical pre-compression load, opening size and ratio, among many other factors. Typically, the mortar joints and unit-mortar interfaces are the weak planes where we expect to observe most failures, such as sliding, cracking and joint opening. However, it is not a straightforward task to simulate the structural behaviour and the failure mechanism of URM walls, including the crack localizations and propagation through the mortar joints, using the standard continuum-based computational models given the composite and highly nonlinear nature of the material. In this context, the present research offers a discontinuum-based approach to simulate the damage progression in URM walls subjected to combined shear-compression loading using the discrete element method (DEM). The masonry walls are represented via distinct elastic blocks interacting through point contacts to their surroundings. It is aimed to present the effect of the local fracture mechanism on the macro response of the masonry walls via validated DEM-based numerical models that can address all possible fracture mechanisms occurring at the unit-mortar interfaces. An innovative damage monitoring technique relying on the stress state at the point contacts is implemented and utilized to explore the associated damage progression in URM walls. The results show the great potential of the adopted modelling strategy to better understand the mechanics of URM walls and indicate the effect of strength properties of masonry constituents on the overall in-plane capacity of the load-bearing walls.

Keywords: Discrete element method, contact mechanics, masonry, in-plane behaviour, fracture mechanisms.

Note:
- This paper was received on July 7, 2023 and accepted for publication by the Editorial Board on December 28, 2023.
- Discussions on this paper will be accepted by July 31, 2024.
- https://doi.org/10.18400/tjce.1323977

1 Carleton University, Department of Civil and Environmental Engineering, Ottawa, Canada
bora.pulatsu@carleton.ca - https://orcid.org/0000-0002-7040-0734

2 Middle East Technical University, Department of Civil Engineering, Ankara, Türkiye
tuncay@metu.edu.tr - https://orcid.org/0000-0002-4523-2388

* Corresponding author

1. INTRODUCTION

The unreinforced masonry (URM) constitutes the vast majority of old building inventory in major cities and rural areas, including historic buildings and most landmark structures. Specifically, masonry refers to a construction technique where the discrete units (or blocks) are laid on top of each other with or without using a binding material (i.e., cement or lime-based mortar) to construct a load-bearing wall system. Often, the bricks (or stone blocks) are stronger and stiffer than the mortar and unit-mortar interfaces; hence, the cracks are most likely to develop and propagate through the joints (referred to as strong brick weak joint combination). Given the considerable difference in the mechanical properties of masonry constituents in URM walls, various crack patterns and failure mechanisms can develop under lateral seismic forces such as rocking, sliding and diagonal tensile failure [1]. It is worth noting that there may be an interaction between the failure modes when a URM wall starts to displace and get damaged [2]. In other words, the structural behaviour of masonry walls may demonstrate progressive damage by switching from one mechanism to another with increased lateral displacement.

With the advances in computational power, different numerical approaches and modelling strategies have been proposed to simulate the in- and out-of-plane response of masonry walls [3]. By and large, continuum-based methods (such as standard Finite Element Analysis, FEA) are commonly used in the structural analysis of URM walls (also referred to as macro-modelling), offering a practical solution with low computational cost and requiring a relatively lower number of input parameters. In macro models, homogenized material properties are used with no distinction among masonry units and mortar, where the material failure is smeared out through the continuous medium [4–7]. Although this approach provides valuable information regarding the overall performance of large-scale buildings and load-bearing wall systems, it may not capture the local mechanisms and crack patterns that are also related to the morphological features of URM walls. Alternatively, discontinuum-based methodologies can be adopted in the seismic analysis or performance assessment of masonry structures. Among different discontinuum-based analyses, the discrete element method (DEM) has been the one that has attracted the most attention from the academic community and industry for the last several decades (*e.g.*, [8–15]). In DEM, the discontinuous texture of masonry is represented explicitly, considering masonry units via rigid or deformable blocks that can interact with each other along their boundaries, as shown in Figure 1. Moreover, the bond between the mortar and the masonry units is denoted as zero-thickness interfaces without including the mortar joint in the numerical formulation (see Figure 1b), which is called simplified micro-modelling (SMM) in the literature [16]. This approach offers a good compromise in accuracy and computational cost that mainly requires reliable input data regarding the bond (or unit-mortar interface) parameters and unit properties. In SMM, the cracking of masonry units is addressed by defining a potential crack surface between adjacent blocks representing a masonry unit, which is also illustrated in Figure 1c. It is important to highlight that the consideration of potential crack surfaces in masonry units, implementation of sophisticated material models, and contact constitutive laws in DEM-based models (both in two- and three-dimensional settings) are driven by expectations from computational predictions. The available studies adopting DEM as a predictive numerical model (e.g., [17–20]) consist of different improvements and simplifications related to the necessities stemming from physical realities. A review article

focusing on the differences between available DEM-based computational models and their application to masonry structures is discussed in [21].

This research follows the SMM approach implemented within the DEM framework, where elastic blocks are used for bricks that can mechanically interact at the contact points to better understand the progressive damage mechanism in unreinforced masonry walls. While previous studies have discussed the accuracy of the DEM-based computational models and the predicted failure mechanisms, they rarely explore the damage progression at the units and the unit-mortar interfaces. To this end, we aim to provide a deeper understanding of the mechanics of URM walls using validated discrete element models and offer a generalized perspective regarding the accumulated damage and its correlation with the lateral load carrying capacity.

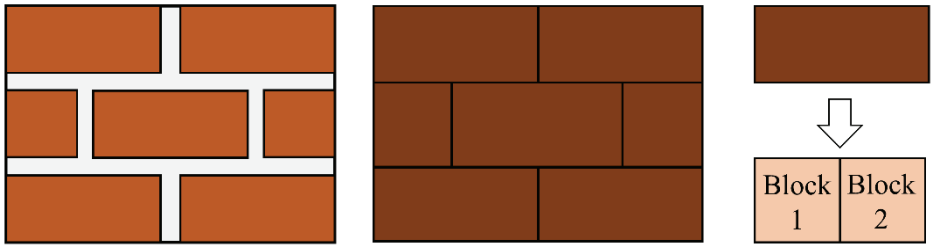

Figure 1 - Representation of masonry wall within the DEM framework; (a) a masonry wall texture, (b) SMM realization and (c) potential crack line (or surface in 3D) for a single block in DEM.

The present study includes the mathematical background of the adopted computational model and validation of the implemented approach by comparing the numerical findings against two experimental results. Then, a detailed investigation is performed to explore the damage progression under the increasing lateral deflection, together with comprehensive sensitivity analyses. Finally, the proposed modelling strategy is applied to simulate the damage progression of a masonry panel with an opening under vertical loading.

2. SIMPLIFIED MICRO-MODELLING VIA DISCRETE ELEMENT METHOD (DEM)

The adopted discontinuum-based approach was initially proposed by Cundall to solve slope stability and rock fragmentation problems [22]. Later, the DEM was used to analyze masonry structures subjected to quasi-static and dynamic loading, among other subjects related to various engineering disciplines. This study performs DEM-based analysis to simulate different URM walls under combined compression-shear loading and predict their structural behaviour from the elastic regime up to failure. A commercial three-dimensional discrete element code, 3DEC developed by Itasca Consulting Group [23], is used during the analyses. The proposed computational modelling approach utilizes elastic blocks, discretized into constant strain tetrahedral (CST) volumes (each consists of four nodes – or gridpoints), and

their mechanical interaction is predicted by computing action/reaction forces at the point contacts (also called sub-contacts) defined along the contact surface, as shown in *Figure 2*.

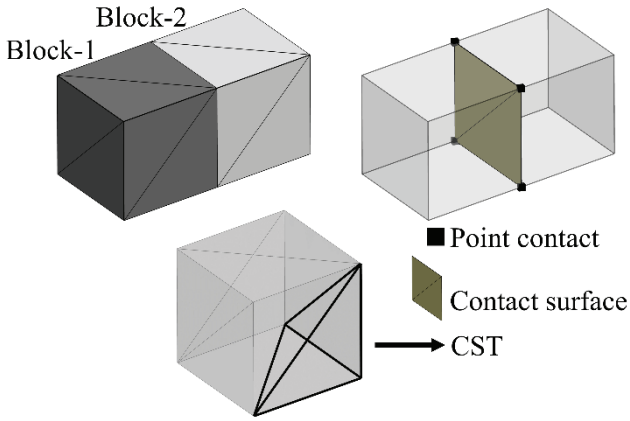

Figure 2 - Two deformable blocks and the contact surface.

The block deformation is computed by solving the equations of motion for each gridpoint (or node) using the central difference algorithm. New nodal velocities are obtained following compact expression at each time step, given in Equation 1. Note that the quasi-static solutions are obtained by adopting Cundall's local damping formulation [24], and the nodal velocities ($\dot{u}_i$) are evaluated at the mid-time intervals (*i.e.*, Δt: time step, $t^+ = t + \Delta t/2$, $t^- = t - \Delta t/2$).

$$\dot{u}_i^{t+} = \dot{u}_i^{t-} + \frac{\Delta t}{m}\left(\Sigma F_i^t - \alpha|\Sigma F_i^t|sgn(\dot{u}_i^{t-})\right) \tag{1}$$

where ΣF_i, m and α are the total force vector, nodal mass (the total mass of a tetrahedron divided by four) and the non-viscous damping constant (default value is 0.8). The sum of forces includes gravity loads, external loads, contact forces (if any), and nodal contribution of the internal stress in the zones adjacent to the gridpoint. Once the new nodal velocities are obtained, nodal displacements are calculated (*i.e.*, $u_i^{t+} = u_i^t + \Delta t(\dot{u}_i^{t+})$), later utilized to predict the block deformation and the relative point contact displacements among the adjacent blocks. In *Figure 3*, the relative displacement of two elastic blocks, in normal and two shear directions, are illustrated. It is worth noting that the point contacts are defined at the vertices of the tetrahedral elements associated with the contact planes. At each contact point, three orthogonal springs are assigned, and the action/reaction forces are computed in the normal and shear directions accordingly. Elastic response at the contact points is governed by the normal and shear contact stiffnesses (k_n, k_s), whereas the failure is controlled by the given tensile (f_t) and compressive (f_m) strength in the normal direction, cohesion (c) and friction angle (θ) in the shear directions. It is important to recall that the normal (σ) and shear (τ) contact stresses are functions of relative normal (u_n) and shear ($u_{s,i}$) displacements. The contact stresses are obtained by first computing elastic increments (*i.e.*, $\Delta\sigma = k_n\Delta u_n$, $\Delta\tau_i = k_s\Delta u_{s,i}$), which are then added to contact stresses computed in the previous time step. Next,

they are corrected (if required) following the defined failure criterion and multiplied with the associated sub-contact area to get forces that are finally used in the equations of motion (Equation 1).

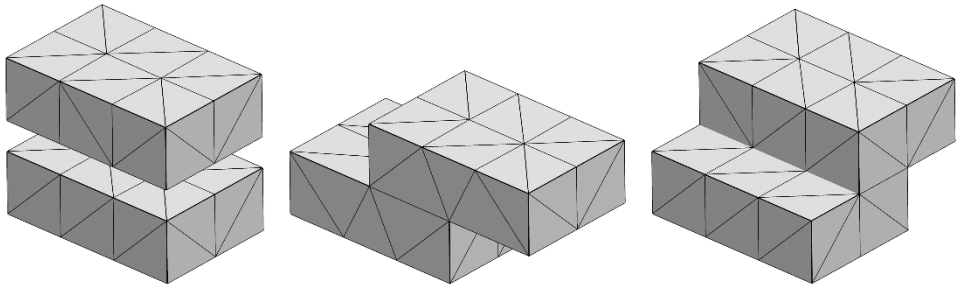

(a) *(b)* *(c)*

Figure 3 - Relative displacement of two blocks: (a) pure tension and (b-c) shear directions.

Throughout this work, recently developed fracture energy based elasto-softening contact constitutive models are used [25]. A bilinear stress-displacement behaviour is implemented in tension, shear and compression regimes, considering the mode-I, mode-II and compressive fracture energy, respectively. The readers can find the graphical representation of implemented contact models in Figure 4a and Figure 4b. The strength reduction (or damage) is imposed in tension, compression and shear strength depending on the recorded relative displacement at the associated point contacts in the normal and shear directions. A single damage parameter is considered to couple tension and shear failure, whereas one-way coupling is considered between shear and compression. The readers are referred to the reference study for a comprehensive discussion and mathematical background of the implemented contact constitutive law [25].

The adopted contact model in the normal direction represents the bond behaviour when subjected to tension, whereas it corresponds to masonry composite behaviour in compression. Therefore, the parameters f_t and f_m denote the bond tensile strength and the compressive strength of the masonry composite, respectively. Upon failure in tension or compression, contact stiffness degradation is considered in the unloading response, which returns to the origin, similar to standard continuum damage mechanics formulation. In shear, the Mohr-Coulomb failure criterion is used, in line with similar studies published in the literature (e.g., [26–30]) that can fairly address the bond shear capacity, where initial and residual bond shear strength (τ_0, τ_{res}) is calculated using cohesion and friction angle parameters (*i.e.*, $\tau_0 = c_0 + tan\theta_0\sigma,\ \tau_{res} = c_{res} + tan\theta_{res}\sigma$). No stiffness degradation is considered for shear stiffness in the pre- and post-peak behaviour. The compression-shear interaction is controlled by the Cap Model, proposed in [31], which is implemented in the DEM framework and presented in *Figure 4*c. The adopted composite yield surface includes tension, compression, and shear failure surfaces, as shown in *Figure 4*.

The explicit solution scheme of DEM is executed in a cyclic manner, such that quasi-static solutions are obtained once the unbalanced force (ΣF) is below the pre-defined threshold (*e.g.*, $|\Sigma F| < 1e-5$ N) or monitored displacements converge to a specific value. Note that

the adopted central difference algorithm only provides stable solutions if the time steps are smaller than the critical value. This condition is automatically satisfied in 3DEC, using sufficiently small time steps, detailed in the reference [32]. On the other hand, the mentioned contact models are implemented in the visual studio environment and compiled as DLL (dynamic link library) in 3DEC. In the following section, the benchmark studies and the application of the DEM are presented.

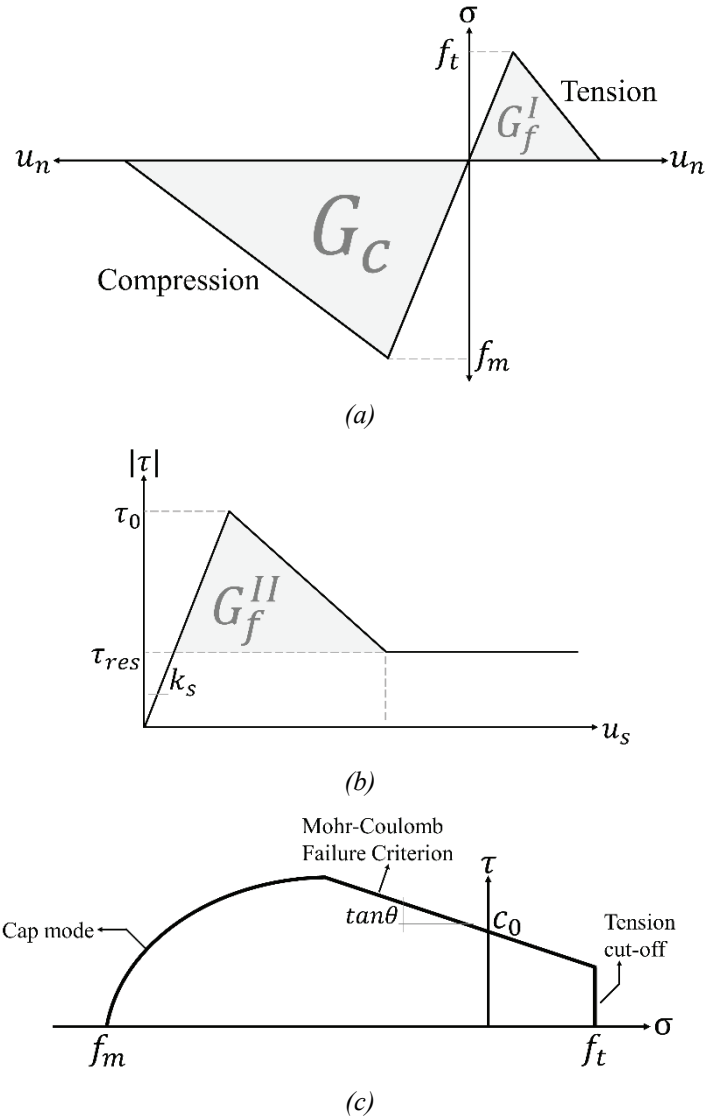

Figure 4 - (a) Contact constitutive law in tension and compression, (b) shear and (c) adopted composite yield surface.

3. VALIDATION STUDIES AND DISCONTINUUM-BASED ANALYSIS

This section presents the experimental studies used as benchmarks to validate the proposed computational modelling strategy. The first reference test was performed by Vermeltfoort et al. [33], exploring the lateral response of URM wall panels ($0.99 \times 1.00 \times 0.098\, m^3$) subjected to combined compression-shear loading with different vertical pressures. Once the vertical loads were applied at the top section of the masonry walls using a solid loading beam, the lateral loads were introduced incrementally by controlling the lateral displacement at the top. No rotation was allowed at the top beam during the lateral loading. This test was already used as validation in an earlier study [20]. Therefore, only a summary of this validation case will be presented here.

In order to study the effect of the local fracture mechanism on the behaviour of masonry walls more precisely, a new validation case was needed to show that the DEM has the capacity to predict damage progression for walls with different aspect ratios. The second benchmark study was presented by Ganz and Thürlimann [34], in which the URM walls consisting of a masonry panel ($3.6 \times 2.0 \times 0.15\, m^3$) and two flanges ($0.15 \times 2.00 \times 0.60\, m^3$) were tested under in-plane loading. Similar to the first reference study, different levels of vertical loads were considered during the testing campaign, causing different lateral load carrying capacities and fracture patterns. In the second benchmark study, the concrete slab was placed at the top of the specimens, where the lateral load was applied during the testing without imposing any restraint on the rotational degrees of freedom of the slab. In Figure 5, the computational models of the reference studies are illustrated. The readers are referred to the references for further details regarding the benchmark tests [33,34].

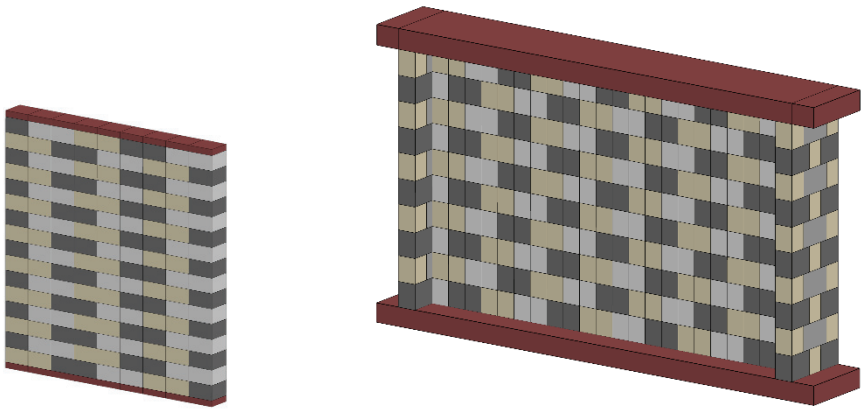

(a) *(b)*

Figure 5 - Illustration of the benchmark studies: (a) Solid wall panel – Benchmark #1, (b) URM wall with flanges – Benchmark #2.

The proposed computational models require the elastic properties of bricks (*i.e.*, Young's modulus and Poisson's ratio) and elasto-plastic properties of the unit-mortar interface (bond), mentioned earlier in Section 2. Typically, bond shear characteristics can be obtained from direct shear testing of masonry couplet or triplet, whereas bond tensile strength can be noted

via direct tension or flexural testings. In this research, brick and bond properties are taken from the provided material characterization tests or previously published academic articles that are in line with the presented modelling strategy [5,31,33–36]. In *Table 1*, assigned material and contact properties are given.

Table 1 - Material and contact properties adopted in the proposed computational models for benchmarks #1 and #2.

Benchmark Study #1					
Masonry Unit Interaction					
E, v (GPa, -)	k_n, k_s (Pa/m)	f_T (MPa)	c_0, c_{res} (MPa)	θ_0, θ_{res} (°)	G_f^I, G_f^{II} (N/m)
16.7, 0.15	820,360	2.0	$1.4f_T$, 0.0	45, 45	80, 500
Unit-Mortar Interface Properties (Bond) - $\boldsymbol{\sigma_v = 1.21, 2.12}$ **MPa**					
k_n, k_s (GPa/m)	f_T, f_m (MPa)	c_0, c_{res} (MPa)	θ_0, θ_{res} (°)	G_f^I, G_f^{II}, G_c (N/m)	C_s (-)
82, 36	0.16, 11.5	$1.4f_T$, 0.0	35, 35	12, 50, 5000	9
Unit-Mortar Interface Properties (Bond) – $\boldsymbol{\sigma_v = 0.30}$ **MPa**					
k_n, k_s (GPa/m)	f_T, f_m (MPa)	c_0, c_{res} (MPa)	θ_0, θ_{res} (°)	G_f^I, G_f^{II}, G_c (N/m)	C_s (-)
82, 36	0.25, 10.5	$1.4f_T$, 0.0	35, 35	12, 125, 5000	9
Benchmark Study #2					
Masonry Unit Interaction					
E, v (GPa, -)	k_n, k_s (Pa/m)	f_T (MPa)	c_0, c_{res} (MPa)	θ_0, θ_{res} (°)	G_f^I, G_f^{II} (N/m)
10, 0.2	100,40	1.5	$1.5f_T$, 0.0	37, 37	22.5, 225
Unit-Mortar Interface Properties (Bond) - $\boldsymbol{\sigma_v = 0.61, 1.91}$ **MPa**					
k_n, k_s (GPa/m)	f_T, f_m (MPa)	c_0, c_{res} (MPa)	θ_0, θ_{res} (°)	G_f^I, G_f^{II}, G_c (N/m)	C_s (-)
20, 8	0.15, 7.6	$1.5f_T$, 0.0	37,37	2.25,150,11500	9

The same loading procedure is applied in the discontinuum models for both benchmark studies, where a constant lateral displacement rate (*i.e.*, 0.005 m/s) is prescribed at the top loading beam after the equilibrium is reached under the self-weight and the vertical pre-compression forces. The base reaction is recorded during the analyses by summing up the shear forces at the springs defined between the supporting block and the bottom course of masonry. In the first benchmark study, three pre-compression loads were considered (*e.g.*,

$\sigma_v = 0.3, 1.21$ and 2.12 MPa). The predicted force-displacement curves and the experimental findings are presented in *Figure 6*. A good agreement is found in comparing the numerical and experimental results in terms of overall force-displacement behaviour and load-carrying capacity. The difference in ultimate lateral load is negligible for low and medium pre-compression pressures ($\sigma_v = 0.3$ MPa and $\sigma_v = 1.21$ MPa), whereas slightly higher capacity, approximately 10%, is noticed for high pre-compression pressure ($\sigma_v = 2.12$ MPa).

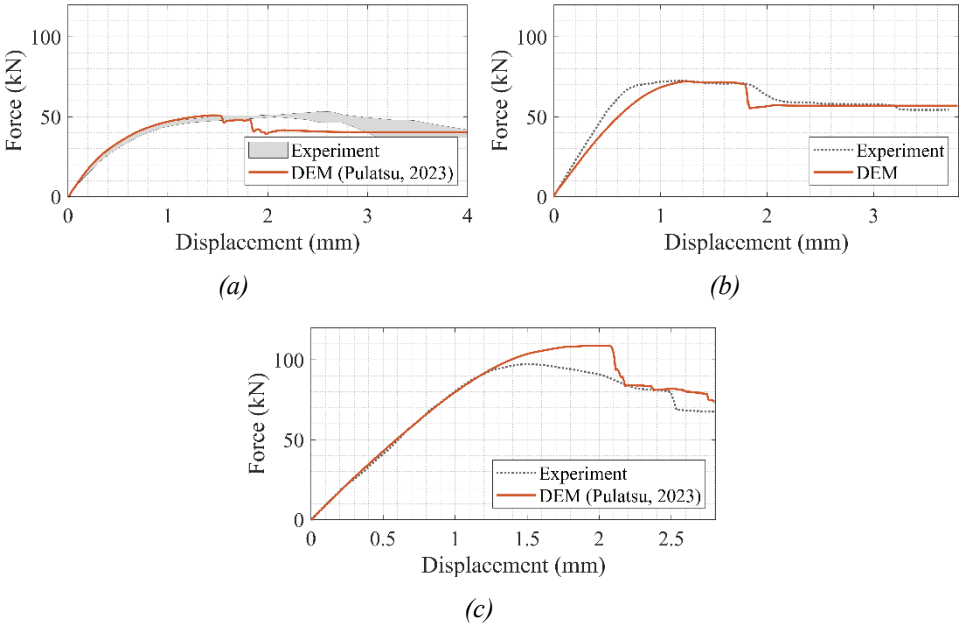

Figure 6 - Comparison of the experimental results (benchmark #1) and the discrete element models for different vertical pre-compression pressures: (a) $\sigma_v = 0.3$, (b) $\sigma_v = 1.21$ and (c) $\sigma_v = 2.12$

Furthermore, the predicted kinematic mechanisms align with the experimental findings, as shown in *Figure 7*. The obtained crack patterns are presented in *Figure 7*b for low, medium and high pre-compression pressures when the force-displacement curves at the ultimate displacement, noted as 4 mm, 3.8 mm and 2.8 mm, respectively. The overall structural behaviour is found to be influenced by the level of pre-compression pressure, which not only controls the maximum lateral load but also affects the damage in bricks (*i.e.*, cracking or combined shear and tensile failure) and the number of failures noted at the unit-mortar interfaces. In *Figure 7*b, the damage computed at the bricks and bonds is represented via points with different colours (*i.e.*, blue: brick failure, black: bond failure) at the locations where the failure occurred. The term "*failure*" is used to describe capacity loss at the point contact, which can no longer transfer action/reaction forces in tension and shear. Hence, we address a local failure at the contact planes. As seen in *Figure 7*b, the number of brick failures is almost double for a high vertical pre-compression pressure ($\sigma_v = 1.21$ MPa) and more

spread to the head joints. Conversely, a distinct localized diagonal tension crack is obtained for a low-pressure ($\sigma_v = 0.30$ MPa), shown in *Figure 7*b.

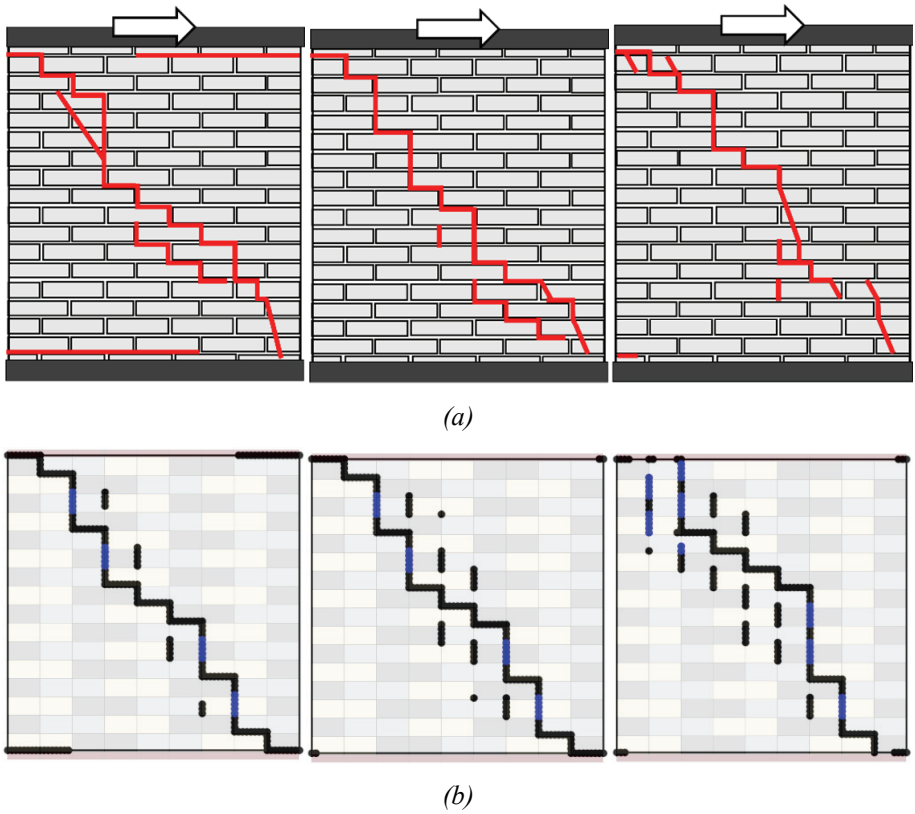

(a)

(b)

Figure 7 - Failure mechanisms obtained from numerical models and experiments (from left to right, $\sigma_v = 0.3, 1.21$ and 2.12 MPa): (a) representation of the crack pattern (test observations), (b) crack pattern obtained from DEM (blue dots indicate cracks in bricks, black dots denote bond failure).

The second benchmark study is a large-scale test and has a different configuration, including masonry wall flanges at both ends. The experimental setup is explicitly represented via the adopted three-dimensional computational model considering the same loading condition and protocol. The results of the proposed discontinuum-based models are compared against the experimental findings, as shown in *Figure 8*a, where low and high pre-compression conditions are denoted as W1 and W2, respectively. A very good match is obtained for W1 with almost no difference in ultimate lateral load, whereas a higher capacity is noted for W2 (approximately 15%) with similar force-displacement behaviour. The predicted crack pattern and the associated failure mechanisms are also given in *Figure 8*b-c, corresponding to the ultimate lateral displacement of 14 mm and 8 mm for W1 and W2, respectively. Almost no brick failure is noticed when the pre-compression pressure is low (W1, $\sigma_v = 0.61$ MPa) as

opposed to W2 that can be seen in *Figure 8*b. In both case studies, diagonal tensile failure is obtained at the final stage of the analyses. Moreover, a moderate crushing failure is also noticed at the bottom right toe in each simulation, as depicted in *Figure 8*.

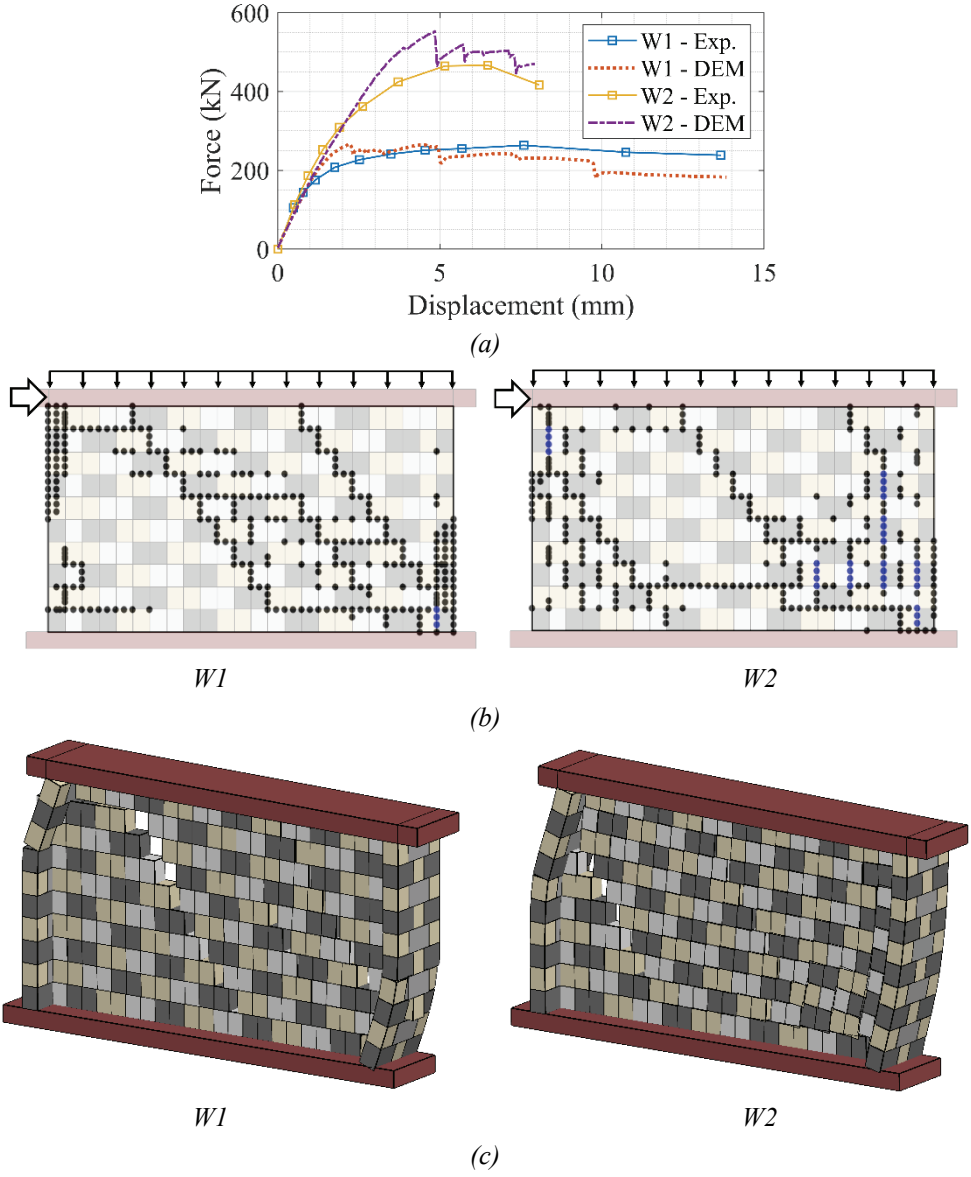

Figure 8 - Comparison of DEM results against the benchmark study #2: (a) Force-displacement curves, (b) crack pattern obtained from DEM (blue dots indicate cracks in bricks, black dots denote bond failure), and (c) predicted failure mechanisms from DEM.

4. DAMAGE PROGRESSION AND SENSITIVITY ANALYSIS

This section aims to provide a deeper understanding of the damage progression in the analyzed URM walls, referred to as benchmark #1 and #2. During the numerical analyses, the state of point contacts is recorded at every 0.2 mm displacement increment to keep track of the damage progression together with the base-shear force and maximum lateral displacement at the top corner. In *Figure 9*, the predicted point contact failures, separately denoted for units and unit-mortar interfaces, are presented for low, medium and high pre-compression pressures for benchmark study #1. The given snapshots are determined based on the observed significant events, such as changes in the crack pattern and the associated failure mechanisms. For instance, in the case of low-pressure ($\sigma_v = 0.3$ MPa), the initial significant phenomenon is noted (around $d = 0.6$ mm) at the bottom left and top right corners of the solid masonry panel, where the point contact failure is noticed for the first time due to flexural tensile stresses between the loading beam and URM wall. Then, after 1.0 mm, additional failures at the contact points corresponding to the head joints are obtained. Finally, a diagonal crack is developed, approximately at 3.0 mm, including cracks at the bricks together with the additional head and bed joints (see *Figure 9*a). Note that once the joint failures start to occur at $d = 1.6$ mm, damage at the unit-mortar interfaces accelerate and rapidly yields a diagonal tension crack, and the fully developed kinematic mechanism does not change until the end of the analysis ($d = 4.0$ mm). Different from the first case, medium pre-compression pressure ($\sigma_v = 1.21$ MPa) leads to different crack evolution, where flexural openings (or cracks) at the top right and bottom left corners are considerably less than the previous one, which is initially noticed at $d = 1.4$ mm simultaneously with several head joint openings, shown in *Figure 9*b. Next, the contact failures are spread at the head joints ($d = 1.6$ mm), and a clear diagonal tension crack is obtained when $d = 2.6$ mm. Similarly, at the initial stage of the lateral displacement, high pre-compression pressure ($\sigma_v = 2.12$ MPa) yields almost no flexural openings between the wall and the loading beam, and the cracks are initially developed at the head joints around the mid-height of the wall, displayed in *Figure 9*c. The final damage state is obtained less than a 1 mm lateral displacement after the head joint cracks are noticed. Furthermore, the results show more brick failures associated with the high vertical pre-compression load compared to the other two pre-compression loads. The given set of solutions underlines the importance of vertical pressure on the observed crack pattern, which also has a favourable influence on the lateral resistance of the URM wall. It needs to be stressed that the analyzed URM walls do not suffer from poor compressive strength, and no fully crushed contact point, meaning no force-transfer capacity in the compression, is computed in all simulations. However, this phenomenon will be an important factor for masonry walls with low compressive strength material characteristics and is out of the scope of the present research.

To quantitatively investigate the relationship between force-displacement behaviour and the associated damage evolution in the bricks and unit-mortar interfaces, they are given in the same plot for all three vertical pre-compression loads, as shown in Figure 10. As mentioned earlier, the two-way coupling mechanism is considered for tension and shear at the contact points using a single damage parameter (denoted as d^{ts}). During analysis, the stress state at the contact points is monitored, and damage at the bricks (d_B^{ts}) and bonds (d_J^{ts}) are recorded

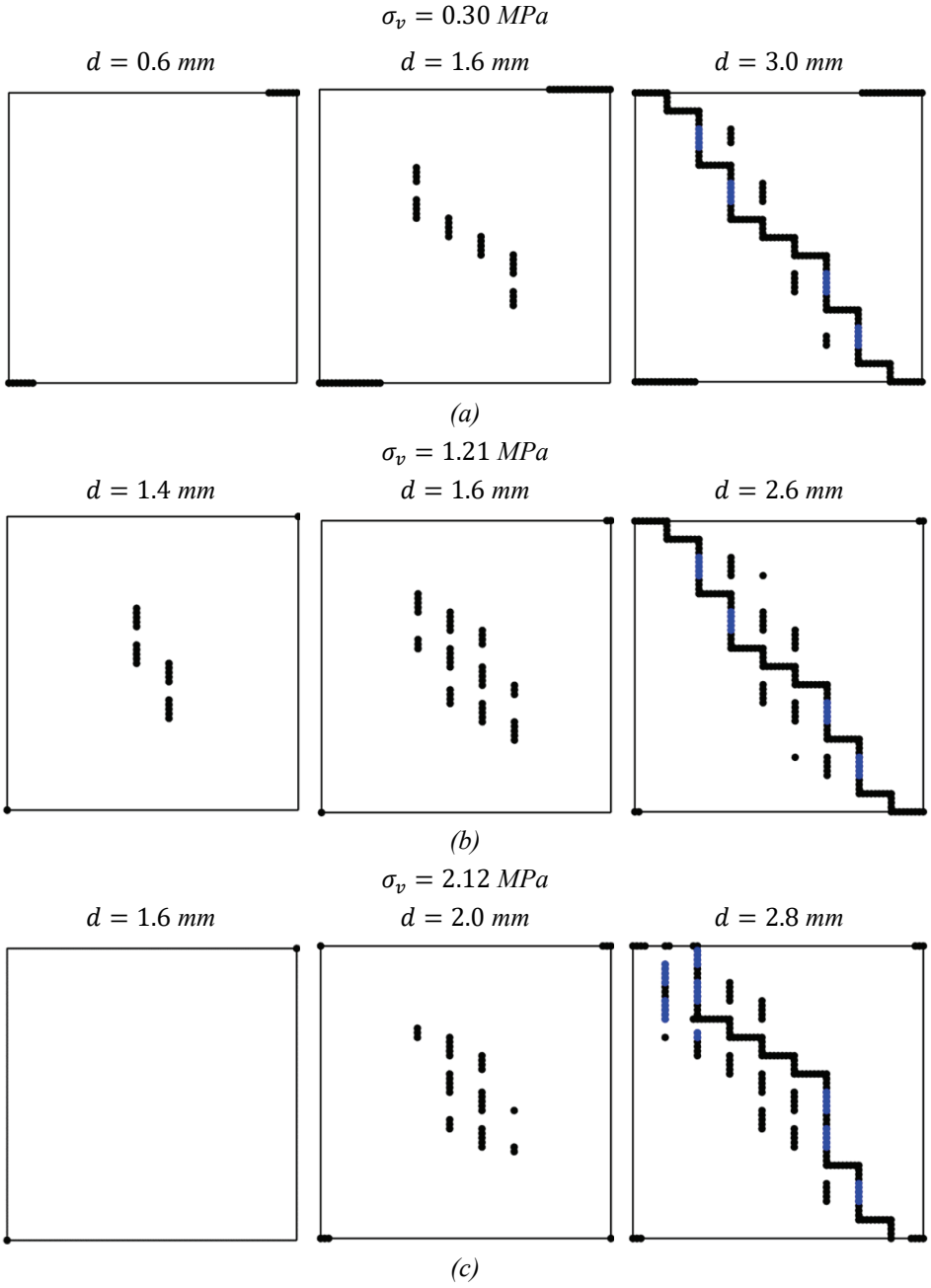

Figure 9 - Results of discontinuum analysis of URM walls (Benchmark #1) for different lateral displacements.

separately. At the end of the analysis, the total number of broken contact points (meaning that d_B^{ts} or d_J^{ts} equal to 1) is calculated, and it is used to present accumulated damage. In *Figure 10*, cumulative damage predicted at the brick and bond contact points is presented together with the force-displacement response of the URM wall. According to the results of the analyses, it is evident that the bond failures (*e.g.*, opening, sliding) start prior to the cracking of bricks, which essentially governs the force drop, hence the lateral load resistance of the URM wall. This conclusion is valid for all pre-compression loads, where the significant capacity loss coincides with the considerable extent of failure in the bricks developing rapidly upon passing the certain displacement threshold. Furthermore, it is interesting to observe that the degradation in the initial stiffness starts with the bond failure at the early stages of the lateral displacement that can be clearly noted for low pre-compression loads and relatively later stages of lateral displacement for high pre-compression loads (see *Figure 10*).

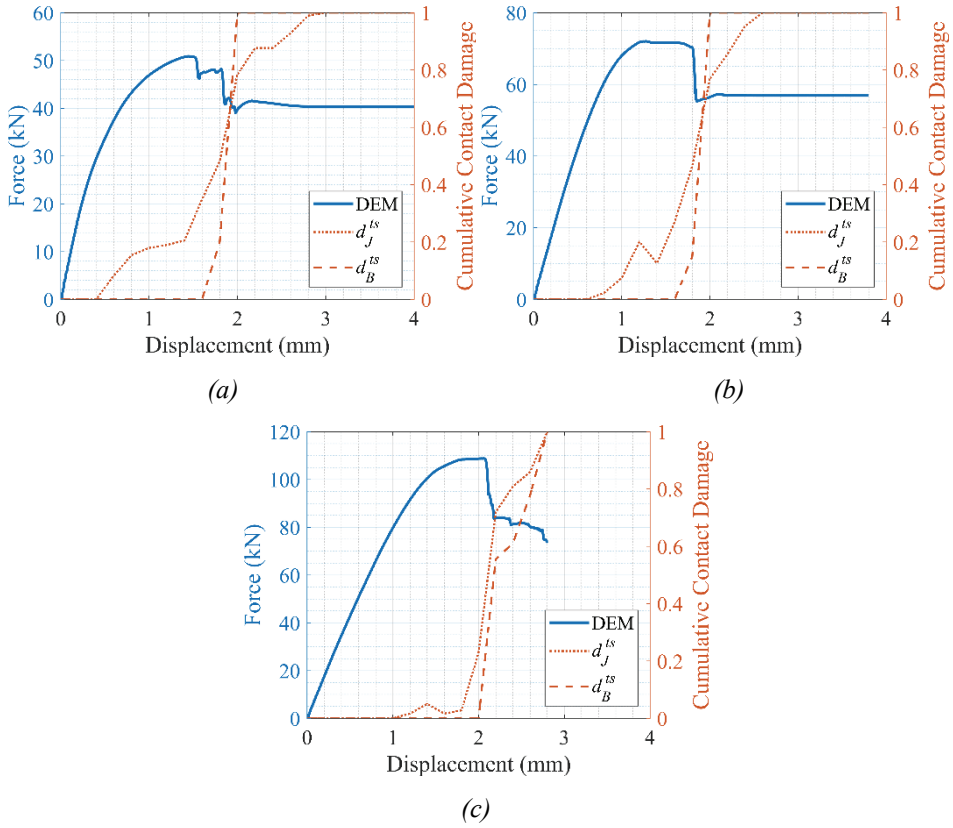

Figure 10 - Combined representation of the cumulative damage at the bricks and joints with the force-displacement behaviour of the URM walls under different vertical pressures (benchmark #1): (a) $\sigma_v = 0.30$ MPa, (b) $\sigma_v = 1.21$ MPa and (c) $\sigma_v = 2.12$ MPa.

The same methodology is applied to the second benchmark study to visualize the cumulative brick and bond damage for W1 and W2, as shown in *Figure 11*. As mentioned previously, very limited tensile cracks are observed in bricks in W1; hence, only the bond failures are displayed in *Figure 11*a. The overall ductile response of W1 and its steady strength reduction upon reaching the maximum load can be attributed to the gradual increase in the joint sliding and openings at the unit-mortar interfaces where each force drop nearly overlaps with the jump in the "*cumulative contact damage*" curve (*Figure 11*a). Similarly, the cumulative brick and bond failures are given in the same graph with the force-displacement response of W2 in *Figure 11*b. The stiffness degradation is initiated by the bond failures, and the lateral load carrying capacity is significantly affected by the brick failure, which is in line with the discussion presented earlier.

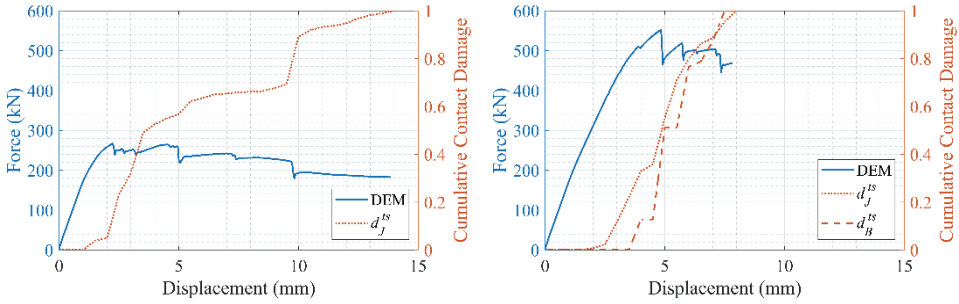

Figure 11 - Combined representation of the cumulative damage at the bricks and joints with the force-displacement behaviour of the URM walls under different vertical pressures (benchmark #2): (a) $\sigma_v = 0.61$ MPa and (b) $\sigma_v = 1.91$ MPa

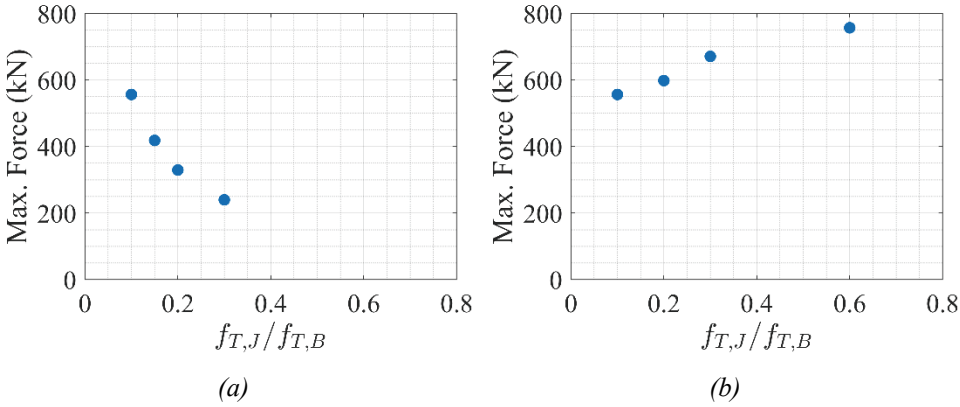

Figure 12 - Influence of the brick and mortar tensile strength on the lateral load carrying capacity of URM wall (benchmark #2): (a) Bond tensile strength ($f_{T,J}$) constant (0.15 MPa) - brick tensile strength ($f_{T,B}$) decreased ↓; (b) $f_{T,B}$ constant (1.5 MPa) - $f_{T,J}$ increased ↑

A further investigation is done using the benchmark study W2 by performing a sensitivity analysis on the brick ($f_{T,B}$) and bond ($f_{T,J}$) tensile strength to predict their effect on the overall lateral resistance of the analyzed URM wall. Two strength combination is considered. First, the brick tensile strength is reduced consistently by keeping the bond strength constant, and then brick tensile strength is kept constant, and bond strength is increased systematically. In *Figure 12*a, the detrimental effect of weak bricks is presented, where an exponential decay can be observed when the brick tensile strength gets lower. Additionally, the positive influence of a strong bond attributed to the higher bond tensile strength can be seen in *Figure 12*b. It is important to recall that no severe crushing failure is computed in the analyzed URM walls. Therefore, the main focus is given to the brick and bond failures that are predominantly related to the tension and shear fracture mechanisms.

5. APPLICATION OF THE PROPOSED STRUCTURAL ANALYSIS FRAMEWORK: URM WALL PANEL WITH AN OPENING

To further validate the implemented modelling approach and demonstrate its applicability on different URM wall sections, the proposed structural analysis framework is also applied to the URM wall panel with an opening subjected to in-plane vertical point load. The analyzed URM panel, tested by Sarhosis et al. [37] to explore the pre- and post-peak behaviour of low bond strength brickwork URM panels with an opening, is illustrated in *Figure 13*. The physical model represents a typical unreinforced brickwork panel above windows and doors in a masonry building. In the reference study, the same experimental configuration was used to perform destructive testing on four URM panels (denoted as S1, S2, S3 and S4), where the vertical loads were imposed at the mid-length of the clear span (l), as shown in *Figure 13*.

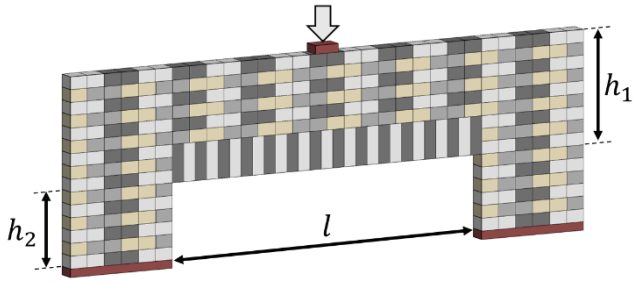

Figure 13 - Analyzed URM wall panel with an opening, where $l = 2.025$ m, $h_1 = 0.675$ m and $h_2 = 0.45$ m.

According to the experimental findings, a similar ultimate load was noted, ranging from 4.6 to 5.6 kN, except for sample S1, which failed earlier than others; hence, it is not considered here when comparing the numerical predictions against the test results. Moreover, experimental observations revealed that failures only occurred along the unit-mortar interfaces, which can be related to the lack of confinement on URM piers and low bond strength. Therefore, no potential crack plane within the masonry units is defined during the discontinuum analysis, which simplifies the computational model and reduces the number of input parameters. The adopted material and contact properties, given in Table 2, are obtained

from the provided experimental results in the reference studies and recommended values in the literature [37–39]. Elastic modulus and Poisson's ratio of the masonry units are taken as 6 GPa and 0.14, respectively. In line with previous validation studies, we utilized the coupled elasto-softening contact constitutive laws, including the mode-I and mode-II fracture energies in tension and shear regimes, respectively.

Table 2 - Material and contact properties used in a masonry panel with an opening.

Masonry Panel with an Opening					
Unit-Mortar Interface Properties (Bond)					
k_n, k_s (GPa/m)	f_T (MPa)	c_0, c_{res} (MPa)	θ_0, θ_{res} (°)	G_f^I, G_f^{II} (N/m)	C_s (-)
13.50, 5.87	0.05	f_T, 0.0	30, 30	0.75, 7.5	9

Figure 14 presents the predicted crack pattern under different load levels, corresponding to noticeable changes in the damage condition. The first crack is captured at the mid-span (above the opening), caused by the flexural tensile stresses due to the effect of vertical point load (1.6 kN), shown in Figure 14a. Upon further increase in vertical load, horizontal cracks develop along the bed joints on both sides of the URM panel (Figure 14b). Ultimately, a diagonal stair-step crack is obtained at the near collapse state of the panel, which initiates along the bed joints and progresses towards the vertical load and the flat-arch skewback, indicated in Figure 14c. The predicted mechanical behaviour of the analyzed URM wall panel with an opening aligns well with the experimental outcomes presented in Figure 14d and Figure 14e.

In addition to the qualitative assessment of the predicted crack pattern, a quantitative comparison of the computational model against the experimental results is provided in *Figure 15*. The force-displacement response obtained from DEM demonstrates a good agreement compared to the experiments, where the specific damage conditions are noted as a, b, and c associated with *Figure 14*a-c. The predicted near-collapse state of the URM panel (see *Figure 15*b) represents the similar failure mechanisms noticed during the experimental campaign.

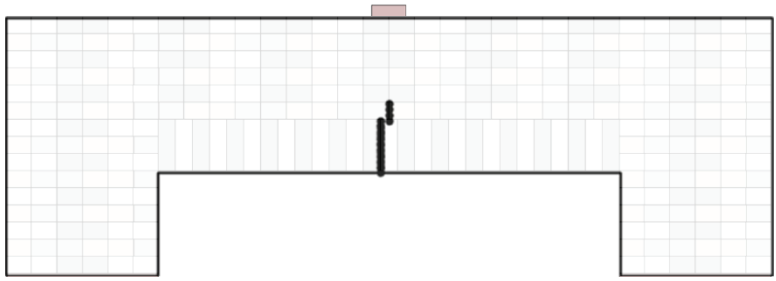

(a)

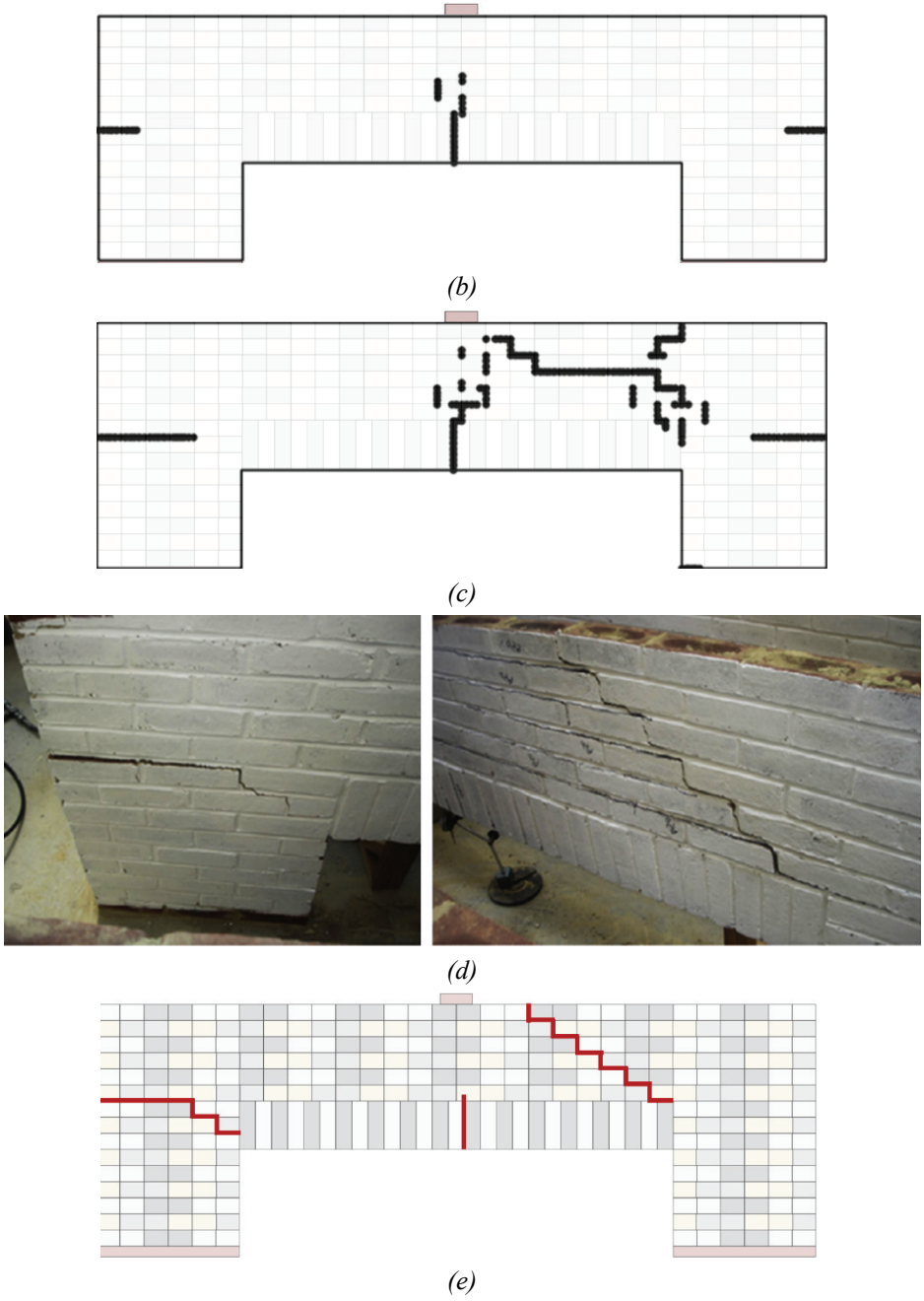

Figure 14 - Predicted damage progression using the proposed DEM-based modelling strategy under different vertical load levels: (a) 1.6 kN, (b) 3.1 kN and (c) 3.44 kN (after peak load) - (d) cracks noted during the experiments [39], (e) representation of the major cracks depicted from reference study.

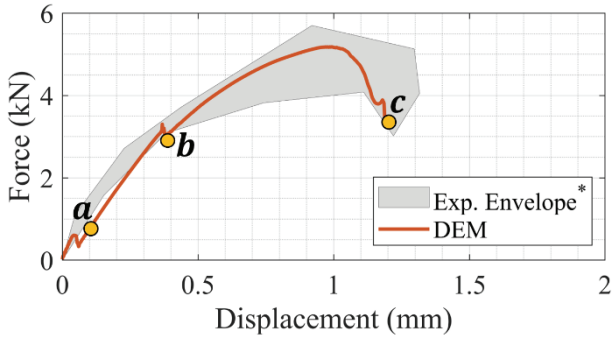

(a)

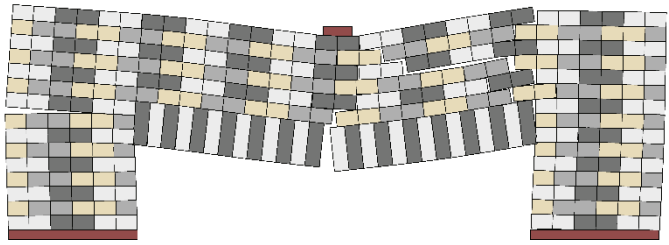

(b)

Figure 15 - (a) Comparison between experimental results denoted as envelope covering three tests (S2, S3 and S4); (b) Predicted near collapse state of the URM panel corresponding to point c in the force-displacement curve.

6. CONCLUSIONS

The present study explores the in-plane behaviour of unreinforced masonry walls via a discontinuum-based modelling strategy based on the discrete element method. The proposed approach captures all essential local failure mechanisms at the bricks and unit-mortar interfaces in tension, compression and shear regimes. The validated computational models are further used to monitor crack propagation and the associated strength reduction in the analyzed benchmark studies. The following conclusions are derived according to the results of the numerical investigations:

- The adopted discontinuum analysis framework provides reasonably accurate predictions regarding the lateral load-carrying capacity of URM walls and the corresponding collapse mechanisms by offering an explicit representation of brick and bond failures.
- The proposed post-processing approach, based on the stress state (or condition) of the contact point in DEM, suggests extracting the fully damaged contact points in tension and/or shear to be utilized in damage progression analysis. The given damage monitoring technique can visualize partially or fully developed kinematic

mechanisms and offers a better understanding of the dominant factors in strength reduction in URM walls, as illustrated in the article.

- The proposed post-processing approach utilizing the output of the adopted discontinuum-based analysis enhances the applicability of discrete element models in the structural assessment of URM walls and buildings, providing necessary information regarding the damage propagation and likely crack pattern.
- The computational investigations indicate a strong relationship between lateral load-bearing capacity and cracking of masonry units (or bricks) in URM walls, especially for medium and high pre-compression loads (*e.g.*, $\sigma_v > 1$ MPa). This phenomenon brings up the importance of brick quality and its influence on the lateral load-carrying capacity of URM walls.
- Finally, the detrimental influence of the weak bricks and the favourable effect of stronger bonds on the in-plane load-carrying capacity of URM walls is presented by performing sensitivity analyses on the brick and bond tensile strength.

As a follow-up study, the proposed DEM-based framework will be applied to more complex unreinforced masonry wall systems (*e.g.*, pier-spandrel), and the adopted post-processing approach will be utilized to assess the seismic capacity of the damaged (or *as-is*) condition of masonry walls and buildings.

References

[1] Tomaževič M. Shear resistance of masonry walls and Eurocode 6: Shear versus tensile strength of masonry. Mater Struct Constr 2009;42:889–907. https://doi.org/10.1617/s11527-008-9430-6.

[2] Betti M, Galano L, Petracchi M, Vignoli A. Diagonal cracking shear strength of unreinforced masonry panels: a correction proposal of the b shape factor. Bull Earthq Eng 2015;13:3151–86. https://doi.org/10.1007/s10518-015-9756-8.

[3] Roca P, Cervera M, Gariup G, Pela' L. Structural analysis of masonry historical constructions. Classical and advanced approaches. Arch Comput Methods Eng 2010;17:299–325. https://doi.org/10.1007/s11831-010-9046-1.

[4] Aldemir A, Erberik MA, Demirel IO, Sucuoğlu H. Seismic performance assessment of unreinforced masonry buildings with a hybrid modeling approach. Earthq Spectra 2013;29:33–57. https://doi.org/10.1193/1.4000102.

[5] Lourenço PB, Rots JG, Blaauwendraad J. Continuum model for masonry: Parameter estimation and validation. J Struct Eng 1998;124:642–52. https://doi.org/10.1061/(ASCE)0733-9445(1998)124:6(642).

[6] Gonen S, Soyoz S. Investigations on the elasticity modulus of stone masonry. Structures 2021;30:378–89. https://doi.org/10.1016/j.istruc.2021.01.035.

[7] Lourenço PB. Anisotropic softening model for masonry plates and shells. J Struct Eng 2000;126:1008–16.

[8] Foti F, Vacca V, Facchini I. DEM modeling and experimental analysis of the static behavior of a dry-joints masonry cross vaults. Constr Build Mater 2018;170:111–20. https://doi.org/10.1016/j.conbuildmat.2018.02.202.

[9] Mendes N, Zanotti S, Lemos J V. Seismic Performance of Historical Buildings Based on Discrete Element Method: An Adobe Church. J Earthq Eng 2020;24:1270–89. https://doi.org/10.1080/13632469.2018.1463879.

[10] Lemos J V. Discrete element modeling of the seismic behavior of masonry construction. Buildings 2019;9. https://doi.org/10.3390/buildings9020043.

[11] Malomo D, DeJong MJ, Penna A. Influence of Bond Pattern on the in-plane Behavior of URM Piers. Int J Archit Herit 2019;00:1–20. https://doi.org/10.1080/15583058.2019.1702738.

[12] Pulatsu B, Erdogmus E, Lourenço PB, Lemos J V., Tuncay K. Simulation of the in-plane structural behavior of unreinforced masonry walls and buildings using DEM. Structures 2020;27:2274–87. https://doi.org/10.1016/j.istruc.2020.08.026.

[13] Murano A, Mehrotra A, Ortega J, Rodrigues H, Vasconcelos G. Comparison of different numerical modelling approaches for the assessment of the out-of-plane behaviour of two-leaf stone masonry walls. Eng Struct 2023;291:116466. https://doi.org/10.1016/j.engstruct.2023.116466.

[14] Gonen S, Pulatsu B, Erdogmus E, Karaesmen E, Karaesmen E. Quasi-static nonlinear seismic assessment of a fourth century A.D. Roman Aqueduct in Istanbul, Turkey. Heritage 2021;4:401–21. https://doi.org/10.3390/heritage4010025.

[15] Mordanova A, de Felice G. Seismic Assessment of Archaeological Heritage Using Discrete Element Method. Int J Archit Herit 2020;14:345–57. https://doi.org/10.1080/15583058.2018.1543482.

[16] Lourenço PB. Computations on historic masonry structures. Prog Struct Eng Mater 2002;4:301–19. https://doi.org/10.1002/pse.120.

[17] Damiani N, DeJong MJ, Albanesi L, Penna A, Morandi P. Distinct element modeling of the in-plane response of a steel-framed retrofit solution for URM structures. Earthq Eng Struct Dyn 2023;52:3030–52. https://doi.org/10.1002/eqe.3910.

[18] Szakály F, Hortobágyi Z, Bagi K. Discrete Element Analysis of the Shear Resistance of Planar Walls with Different Bond Patterns. Open Constr Build Technol J 2016;10:220–32. https://doi.org/10.2174/1874836801610010220.

[19] de Felice G. Out-of-plane seismic capacity of masonry depending on wall section morphology. Int J Archit Herit 2011;5:466–82. https://doi.org/10.1080/15583058.2010.530339.

[20] Wilson R, Szabó S, Funari MF, Pulatsu B, Lourenço PB. A Comparative Computational Investigation on the In-Plane Behavior and Capacity of Dry-Joint URM Walls. Int J Archit Herit 2023. https://doi.org/10.1080/15583058.2023.2209776.

[21] Lemos J V. Discrete element modeling of masonry structures. Int J Archit Herit 2007;1:190–213. https://doi.org/10.1080/15583050601176868.

[22] Cundall PA. A computer model for simulating progressive, large-scale movements in blocky rock systems. Int. Symp. Rock Mech., vol. 2, Nancy: 1971, p. 47–65.

[23] Itasca Consulting Group Inc. 3DEC Three Dimensional Distinct Element Code 2013.

[24] Cundall PA, Detournay C. Dynamic relaxation applied to continuum and discontinuum numerical models in geomechanics. Rock Mech. Eng. Vol. 3 Anal. Model. Des., 2017, p. 45–90. https://doi.org/10.1201/b20402.

[25] Pulatsu B. Coupled elasto-softening contact models in DEM to predict the in-plane response of masonry walls. Comput Part Mech 2023. https://doi.org/10.1007/s40571-023-00586-x.

[26] Sarhosis V, Dais D, Smyrou E, Bal İE, Drougkas A. Quantification of damage evolution in masonry walls subjected to induced seismicity. Eng Struct 2021;243. https://doi.org/10.1016/j.engstruct.2021.112529.

[27] Saygılı Ö, Lemos J V. Investigation of the Structural Dynamic Behavior of the Frontinus Gate. Appl Sci 2020;10:5821. https://doi.org/10.3390/app10175821.

[28] Çaktı E, Saygılı Ö, Lemos J V., Oliveira CS. Discrete element modeling of a scaled masonry structure and its validation. Eng Struct 2016;126:224–36. https://doi.org/10.1016/j.engstruct.2016.07.044.

[29] Casapulla C, Mousavian E, Argiento L, Ceraldi C, Bagi K. Torsion-shear behaviour at the interfaces of rigid interlocking blocks in masonry assemblages: experimental investigation and analytical approaches. Mater Struct Constr 2021;54. https://doi.org/10.1617/s11527-021-01721-x.

[30] Pulatsu B, Gonen S, Lourenço PB, Lemos J V., Hazzard J. Computational investigations on the combined shear–torsion–bending behavior of dry-joint masonry using DEM. Comput Part Mech 2022. https://doi.org/10.1007/s40571-022-00493-7.

[31] Lourenço PB, Rots JG. Multisurface interface model for analysis of masonry structures. J Eng Mech 1997;123:660–8.

[32] Lemos J V. Block modelling of rock masses. Concepts and application to dam foundations. Rev Eur Génie Civ 2008;12:915–49. https://doi.org/10.3166/ejece.12.915-949.

[33] Vermeltfoort AT, Raijmakers T, Janssen HJM. Shear tests on masonry walls. In: Hamid AA, Harris HG, editors. 6th North Am. Mason. Conf., Philadelphia: The Masonry Society; 1993, p. 1183–93.

[34] Ganz HR, Thürlimann B. Tests on masonry walls under normal and shear loading. Zurich, Switzerland: 1984.

[35] Lourenço PB, Gaetani A. Recommended properties for advanced numerical analysis. Finite Elem. Anal. Build. Assess., New York: Routledge; 2022, p. 209–320. https://doi.org/10.1201/9780429341564-4.

[36] Wilding BV, Dolatshahi KM, Beyer K. Shear-compression tests of URM walls: Various setups and their influence on experimental results. Eng Struct 2018;156:472–9. https://doi.org/10.1016/j.engstruct.2017.11.057.

[37] Sarhosis V, Sheng Y, Garrity SW. Computational modelling of clay brickwork walls containing openings. Int Mason Soc 2010;11:1743–52.

[38] Giamundo V, Sarhosis V, Lignola GP, Sheng Y, Manfredi G. Evaluation of different computational modelling strategies for the analysis of low strength masonry structures. Eng Struct 2014;73:160–9. https://doi.org/10.1016/j.engstruct.2014.05.007.

[39] Sarhosis V, Garrity SW, Sheng Y. Influence of brick-mortar interface on the mechanical behaviour of low bond strength masonry brickwork lintels. Eng Struct 2015;88:1–11. https://doi.org/10.1016/j.engstruct.2014.12.014.